

# Topology of the Trans-Membrane Peptide WALP23 in Model Membranes under Negative Mismatch Conditions

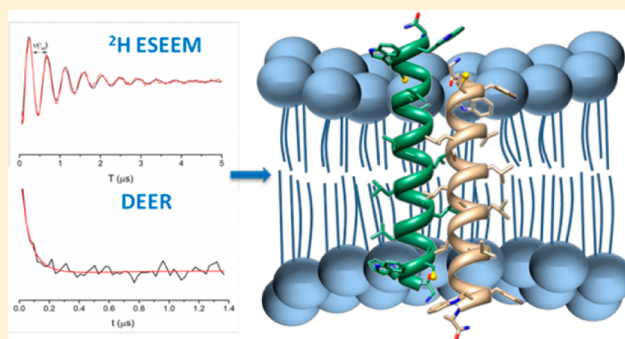
Erez Matalon,<sup>†</sup> Ilia Kaminker,<sup>†</sup> Herbert Zimmermann,<sup>||</sup> Miriam Eisenstein,<sup>‡</sup> Yechiel Shai,<sup>§</sup> and Daniella Goldfarb<sup>\*,†</sup>

<sup>†</sup>Department of Chemical Physics, <sup>‡</sup>Department of Chemical Research Support, and <sup>§</sup>Department of Biological Chemistry, Weizmann Institute of Science, Rehovot, Israel 76100

<sup>||</sup>Max-Planck Institute for Medical Research, 69120 Heidelberg, Germany

## S Supporting Information

**ABSTRACT:** The organization and orientation of membrane-inserted helices is important for better understanding the mode of action of membrane-active peptides and of protein–membrane interactions. Here we report on the application of ESEEM (electron spin–echo envelope modulation) and DEER (double electron–electron resonance) techniques to probe the orientation and oligomeric state of an  $\alpha$ -helical trans-membrane model peptide, WALP23, under conditions of negative mismatch between the hydrophobic cores of the model membrane and the peptide. Using ESEEM, we measured weak dipolar interactions between spin-labeled WALP23 and  $^2\text{H}$  nuclei of either the solvent ( $\text{D}_2\text{O}$ ) or of lipids specifically deuterated at the choline group. The ESEEM data obtained from the deuterated lipids were fitted using a model that provided the spin label average distance from a layer of  $^2\text{H}$  nuclei in the hydrophilic region of the membrane and the density of the  $^2\text{H}$  nuclei in the layer. DEER was used to probe oligomerization through the dipolar interaction between two spin-labels on different peptides. We observed that the center of WALP23 does not coincide with the bilayer midplane and its N-terminus is more buried than the C-terminus. In addition, the ESEEM data fitting yielded a  $^2\text{H}$  layer density that was much lower than expected. The DEER experiments revealed the presence of oligomers, the presence of which was attributable to the negative mismatch and the electrostatic dipole of the peptide. A discussion of a possible arrangement of the individual helices in the oligomers that is consistent with the ESEEM and DEER data is presented.



## ■ INTRODUCTION

Interactions between membrane proteins and lipids are essential to a large variety of cellular processes such as membrane traffic, membrane biogenesis, and signaling. However, the details of protein–lipid interactions in these processes are currently not well understood. This is because lipids and proteins can influence each other in many different ways.<sup>1–3</sup> The effect of lipids may be manifested in membrane protein topologies<sup>4</sup> and structures by changing their side chain orientation or the conformation of the backbone.<sup>2,5</sup> Lipids may also influence the tilt angle of trans-membrane segments of proteins or peptides, driven by a hydrophobic mismatch between the bilayer hydrophobic thickness and the length of the membrane spanning part of the peptide or the protein. Membrane proteins can also affect lipids by varying the lipids' lateral organization, promoting membrane fusion or the trans-bilayer movement of lipids, and stretching or disordering the surrounding lipid chains.<sup>6</sup>

Biological membranes are complex systems due to their composition diversity, and therefore, in biophysical studies they are often represented by simplified model systems in the form of vesicles with well-defined compositions. Similarly, in

protein–membrane studies, proteins are often reduced to smaller molecular entities, such as peptides that preserve a particular aspect of the protein function. The choice of the model system in terms of lipids and peptides is crucial with respect to the information that can be derived. The choice also depends on the techniques that are available to characterize the systems.<sup>1</sup>

Continuous wave (CW) electron paramagnetic resonance (EPR) spectroscopy, combined with spin labeling, is a well-established technique for studying peptide–membrane interactions.<sup>7–9</sup> Recently, long-range distance measurements by pulse double electron–electron resonance (DEER)<sup>10–12</sup> have been used for probing peptides' conformation and aggregation.<sup>13–17</sup> We and others have shown that electron-spin–echo envelope modulation (ESEEM) spectroscopy is another effective EPR technique to study peptide–membrane assemblies,<sup>14,18–21</sup> with particular emphasis on peptide orientation, immersion depth, and water exposure. This method measures

**Received:** October 11, 2012

**Revised:** December 25, 2012

**Published:** January 11, 2013

Table 1. Sequences of Spin-Labeled WALP23 Peptides

label position	peptide name	peptide sequence <sup>a</sup>
4	WALP23C4	GWWC(sl)ALALALALALALALWVA-NH <sub>2</sub>
9	WALP23C9	GWWLALALC(sl)LALALALALWVA-NH <sub>2</sub>
12	WALP23C12	GWWLALALALAC(sl)ALALALALWVA-NH <sub>2</sub>
14	WALP23C14	GWWLALALALALAC(sl)ALALALWVA-NH <sub>2</sub>
17	WALP23C17	GWWLALALALALALALC(sl)LALWVA-NH <sub>2</sub>
20	WALP23C20	GWWLALALALALALALALAC(sl)WVA-NH <sub>2</sub>

<sup>a</sup>C(sl) is a nitroxide-labeled cysteine residue.

weak hyperfine interactions between the electron spin and nearby nuclear spins, which are manifested as modulations in the echo decay.<sup>22–24</sup> We developed an approach in which modulations from <sup>2</sup>H nuclei from D<sub>2</sub>O<sup>21,25</sup> are used to explore water exposure and <sup>2</sup>H nuclei from specifically deuterated phospholipids are employed to probe interactions with different regions of the lipid bilayer.<sup>14,18</sup> Comparison of such ESEEM data obtained for a peptide spin-labeled at different residues provides information about the peptide's orientation and its immersion depth.

This ESEEM strategy has been demonstrated by interacting melittin with model membranes.<sup>14,26</sup> Estimation of the insertion depth of the peptide was based on spin-labeled phospholipids as a reference system. The results, however, led to conflicting estimates because different insertion depths were implied from D<sub>2</sub>O and deuterated lipids.<sup>14,18</sup> This raised the question whether spin-labeled lipids form an adequate reference system for investigating peptide locations in vesicle models. Problems in using spin-labeled lipids in accessibility studies were previously pointed out by Nielsen et al.<sup>27</sup> More specifically, these problems were associated with wide variations in the spin-probe conformation, which complicated the interpretation, and disorder that may be introduced by the label, especially near the bilayer midplane.<sup>28,29</sup> Furthermore, spin-labeled lipids cannot properly account for changes in the modulation depth of spin-labeled peptides that are associated with the peptide's volume. The volume of a spin-labeled peptide inserted into the membrane changes the number of phospholipid molecules in the vicinity of its spin label, thus effectively reducing their local density in this region. This problem can, in principle, be overcome through a quantitative analysis that provides an average immersion depth, thus avoiding the need for empirical ruler altogether.<sup>18</sup>

In the present study, we further demonstrated the use of <sup>2</sup>H ESEEM and DEER as characterization tools to elucidate the structural features of peptide–membrane systems, focusing on the effects of a negative mismatch. For this purpose we used a single trans-membrane  $\alpha$ -helical peptide that comprises a hydrophobic stretch of alternating leucines and alanines flanked at both ends by a pair of tryptophans (WALP).<sup>30</sup> Its membrane orientation was characterized by circular dichroism and IR spectroscopy;<sup>31</sup> it exhibited an  $\alpha$ -helical structure under a range of conditions.<sup>32</sup> The peptide is completely inserted into the membrane due to its unique amino acid composition: leucine, which combines a high predicted helicity with a high hydrophobicity, alanine, which exhibits a high helix-forming propensity, and tryptophan residues, which are utilized as common flanking motifs.<sup>1</sup> Because WALP is a single  $\alpha$ -helix, spin labels introduced periodically along its helical axis can be used to probe different regions of the membrane. Accordingly, WALP23 has already been used as a reference for peptide insertion into membranes based on their accessibility to

paramagnetic quenchers.<sup>27</sup> We used WALP23 in multilamellar vesicles (MLV) consisting of a 7:3 mol ratio of the zwitterionic dipalmitoylphosphatidylcholine (DPPC) and monovalent ion phosphatidylglycerol (PG), respectively. This peptide composition mimics bacterial membranes and is relevant for studying membrane-active peptides.<sup>14,18,33–36</sup> This system also serves as a model for peptide–membrane interactions under negative mismatch conditions, where the hydrophobic core of the peptide is shorter than the hydrophobic layer of the membrane.<sup>1</sup> The nominal peptide/lipid ratio used was 1:200. This ratio is lower than that used in other related EPR studies (1:100)<sup>27,37</sup> as we wanted to ensure insertion of the peptide. In addition, we wanted to minimize spin–spin interactions and thereby prolong the phase memory time and increase the sensitivity of the pulse EPR experiments used in this work.

Here, the ESEEM time domain traces of the deuterated lipid samples were fitted using a model that yields the average distance,  $Z_0$ , of the unpaired electron from a relevant layer with homogeneously distributed <sup>2</sup>H nuclei, and the layer density,  $d$ .<sup>18</sup> We observed that the center of WALP23 was shifted with respect to the bilayer center and that the density of the deuterated layer in the polar head region was unexpectedly small. Moreover, DEER measurements revealed that the peptide formed oligomers within the membrane and that these can account for the unexpectedly small layer density. We discuss possible peptides arrangements, where the N-termini are more buried in the membrane as compared with the C-termini and are consistent with the ESEEM and DEER data. We suggest that the driving force for the discussed peptide topology is the negative mismatch between the membrane and the peptide hydrophobic cores.<sup>1,6,38</sup>

## ■ EXPERIMENTAL METHODS

**Materials.** The phospholipids dipalmitoylphosphatidylcholine (DPPC) (Sigma) and egg phosphatidylglycerol (PG) (Lipid products) were used as received. 1,2-Dipalmitoyl-*sn*-glycero-3-phosphocholine-*N,N,N*-trimethyl-*d*<sub>9</sub> (DPPC-*d*<sub>9</sub>) was synthesized as reported earlier, and the isotopic purity was found to be greater than 98%.<sup>39</sup> MTSL (1-oxyl-2,2,5,5-tetramethyl-3-pyrroline-3-methylmethanethiosulfonate) was purchased from Toronto Research Chemicals, Ontario, CA. 1-Palmitoyl-2-stearoyl-(5-DOXYL)-*sn*-glycero-3-phosphocholine (SPCSL) was synthesized according to the procedure described earlier.<sup>40</sup>

**Peptide Synthesis and Labeling.** The WALP peptides were synthesized by the solid phase method on rink amide MBHA resin (0.22 mequiv/g) by using an ABI 433A automatic peptide synthesizer (peptide names and sequences are presented in Table 1). The principles of peptide–resin cleavage and peptide purification have been described elsewhere.<sup>18</sup> The peptides were labeled with MTSL via a disulfide bridge linker. A 10-fold excess of the radical dissolved in DMSO was used for

labeling. The radical, together with the peptide in DMSO, was agitated at room temperature for 12 h. Spin-labeled peptides were purified by HPLC on a C4 reverse phase column (Vydac 214TP1010). Labeled peptides were shown to be homogeneous by analytical HPLC (>97%, by weight). The labeling was confirmed by mass spectrometry using a Bruker Reflex IIIITM matrix-assisted laser desorption/ionization (MALDI) time-of-flight (TOF) mass spectrometer (MS) (Bruker, Bremen, Germany).

**Preparation of Samples for EPR Studies.** EPR samples were prepared by mixing the peptide and phospholipid stock solutions, yielding a WALP-to-phospholipid molar ratio of 1:200. They were prepared as follows: A dry phospholipid mixture of DPPC/PG (7:3) or DPPC-*d*<sub>9</sub>/PG (7:3) was dissolved in a CHCl<sub>3</sub>/MeOH mixture (2:1, v/v). The WALP peptides were added to the lipid solution, yielding a peptide concentration of 0.2 mM. The lipid–peptide solution was dried using a nitrogen gas stream, followed by vacuum drying overnight. MLV were prepared by hydrating the peptide–lipid film in 0.1 M deuterated or nondeuterated phosphate buffer at pH 7.2. The suspension was mixed on a vortex mixer for 2 min and submitted to 10 freeze–thaw cycles to increase the homogeneity of the vesicles. In addition to WALP peptides in vesicles, a reference system containing phospholipids spin labeled at the fifth carbon in the *sn*-2 chain (SPCSL) in vesicles was also prepared: a dry phospholipid mixture of DPPC/PG (7:3) or DPPC-*d*<sub>9</sub>/PG (7:3) was dissolved in a CHCl<sub>3</sub>/MeOH mixture (2:1, v/v). The SPCSL was added to DPPC/DPPC-*d*<sub>9</sub>/PG (3.5:3.5:3) or DPPC-*d*<sub>9</sub>/PG (7:3) solutions, yielding 1% of the total lipids. The solvents were evaporated under a nitrogen stream followed by vacuum drying overnight. A lipid suspension was prepared by mixing the lipids with nondeuterated phosphate buffer for 2 min and then submitting it to 10 freeze–thaw cycles to yield a final lipid concentration of 5 mg/mL. All samples for ESEEM and DEER measurements (WALP and SPCSL) were prepared as follows: the samples were incubated at room temp for 30 min, to allow the peptide–membrane interaction to equilibrate. Next, approximately 50–60  $\mu$ L were placed into an EPR Teflon tube (2.7 mm i.d. and 3.7 mm o.d.) and rapidly frozen by inserting into liquid nitrogen. Thereafter, the samples remained frozen. From the intensity of the EPR spectra and the extent of the DEER background decay (Figure S14, Supporting Information) as compared to SPCSL we estimated the bulk spin concentration to be  $0.07 \pm 0.01$  mM and not 0.2 mM as introduced. We attribute this to a low efficiency of the peptide incorporation into the membrane, yielding a final peptide/lipid ratio of 1:600.

**CW-EPR Measurements.** All CW X-band (9.5 GHz) measurements were performed at room temperature (22–25 °C) on a Bruker ELEXSYS 500 spectrometer using round quartz capillaries (0.6 i.d. and 0.84 o.d., VitroCom, Inc.).

**ESEEM Measurements.** ESEEM experiments were carried out at 50 K on a Bruker ELEXSYS E580 spectrometer (9.5 GHz) using a ER 4118X-MS-5 probehead with a split ring resonator (5 mm sample access). The ESEEM experiments were performed using the three-pulse sequence  $\pi/2$ – $\tau$ – $\pi/2$ – $T$ – $\pi/2$ – $\tau$ –echo, with time interval  $T$  incremented in 20 ns steps starting at 60 ns, a repetition time of 2.5 ms, and a four-step phase cycle.<sup>41</sup> The magnetic field position was set to the maximum of the nitroxide EPR spectrum; the length of the  $\pi/2$  microwave pulses was 16 ns. The  $\tau$ -value was optimized for maximizing <sup>2</sup>H modulations  $\tau = 1/(2\nu_1) \sim 224$  ns, where  $\nu_1$  is the <sup>2</sup>H Larmor frequency.

**Data Analysis.** Fourier transformation of the ESEEM (FT-ESEEM) trace was carried out as follows: (1) phase correction, (2) normalization, (3) removal of proton modulation using a low-pass frequency filter, (4) division with a fifth-order-polynomial obtained from fitting the echo decay that accounts for electron spin–lattice relaxation,  $T_1$ , during the time interval  $T$ , (5) subtraction of a unity, (6) apodization with a Hamming window, zero filling to 4096 points, FT, and cross-term averaging.<sup>42</sup> All experimental ESEEM traces were treated identically. We chose the intensity of the <sup>2</sup>H peak,  $I(^2\text{H})$ , in the FT-ESEEM as a characteristic of the <sup>2</sup>H ESEEM pattern reflecting the modulation depth, which is in turn, indicative of the <sup>2</sup>H density around the spin label. The calculated ESEEM traces were treated similarly except for multiplication by an extra exponential decay to account for the <sup>2</sup>H quadrupolar interaction ( $T_Q$ ), as will be described in detail later. The  $T_1$  decay was removed from the experimental data, and therefore, it is not considered in the simulations.

In D<sub>2</sub>O suspensions, the <sup>2</sup>H peak consists of a narrow component owing to remote deuterium nuclei,  $I(^2\text{H})_{\text{narrow}}$ , and a broad component owing to water molecules that form H-bonds with the NO group.<sup>43</sup> In the D<sub>2</sub>O samples we used only  $I(^2\text{H})_{\text{narrow}}$ . All ESEEM traces exhibited very weak glitches at  $T = \tau$  owing to incomplete removal of unwanted echoes by the phase cycling. These interfered with data fitting in the case of DPPC-*d*<sub>9</sub>/PG (7:3) in H<sub>2</sub>O, where the modulation depth was low. Therefore, here, the first modulation period (first 20 points in the time domain ESEEM trace) was removed and reconstructed by linear prediction singular value decomposition (LPSVD) prior to the data analysis.<sup>44</sup> Figure S1 in the Supporting Information shows an example of LPSVD performed on a sample of SPCSL in DPPC/DPPC-*d*<sub>9</sub>/PG (3.5:3.5:3). This was done between steps (2) and (3) in the data analysis procedure.

**DEER Measurements.** The constant time four-pulse DEER experiment,  $\pi/2(\nu_{\text{obs}}) - \tau_1 - \pi(\nu_{\text{obs}}) - t - \pi(\nu_{\text{pump}}) - (\tau_1 + \tau_2 - t) - \pi(\nu_{\text{obs}}) - \tau_2$ –echo<sup>45</sup> was carried out at 50 K. The  $\pi/2$  and  $\pi$  pulses of the observer channel were both set to 32 ns. The  $\pi$  pulse of the pump channel was set to 16 ns. A two-step phase cycle was implemented on the first pulse. The pump frequency was set to the maximum of the EPR spectrum and the observer frequency was 65 MHz higher. Accumulation times for the data sets were  $\sim 16$  h. The DEER data were analyzed using DeerAnalysis 2011.<sup>46</sup>

**Theoretical Model.** We present a model for calculating the ESEEM time domain trace of a nitroxide spin label within a membrane. This model allows us to analyze the ESEEM traces quantitatively and to obtain the distances of the spin label from the membrane surface and an average <sup>2</sup>H nuclei density in the vicinity of the spin label. The model simulates a spin label in a membrane composed of phospholipids with a deuterated choline group that is treated as a continuous layer of <sup>2</sup>H nuclei with a homogeneous density,  $d$ . It is assumed that the curvature radius of the MLV is considerably larger than the range of the electron nuclear dipolar interaction that can be accessed by ESEEM. Therefore, the curvature of the vesicle surface can be neglected, and it is treated as an “infinite” flat layer. Finally, the model considers only one leaflet of the phospholipid layers. Namely, a spin label “encounters” only one deuterium layer. This is justified by the lack of <sup>2</sup>H modulation for WALP23 with spin labels buried deep in the alkyl chain region. The model is based on previous work<sup>18</sup> and its geometry is presented in Figure 1.



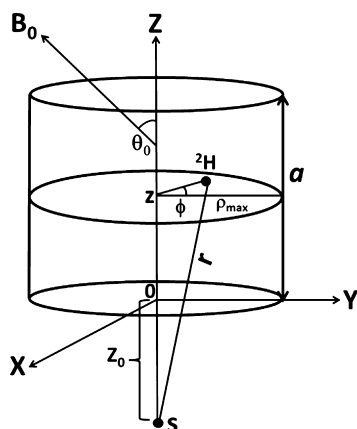


**Figure 1.** Model for calculating the ESEEM trace of an electron spin,  $S$ , situated away from or within a  $^2\text{H}$  nuclei layer. The model assumes a homogeneous distribution of deuterons in the cylinder.

The unpaired electron is situated on the  $Z$  axis (perpendicular to the layer) at position  $Z_0$ , and the deuterium layer is described as a cylinder with radius  $\rho_{\text{max}}$ , a height  $a$ , and the number of  $^2\text{H}$  nuclei in the cylinder is  $N$ .  $Z_0$  is negative when the electron spin is located within the layer or in the solvent part. Obviously, a spin label in a membrane does not have one  $Z_0$  value due to the membrane dynamics and the motion of the MTSL tether. Accordingly, one has to take a range of  $Z_0$  values because of disorder. In our calculation such fluctuations are put effectively in the layer thickness. The coordinates (location) of a particular nucleus in the cylinder are given by  $[\rho \sin \phi, \rho \cos \phi, z]$ ;  $\rho$  is the distance from the  $Z$  axis, and  $\phi$  is the azimuthal angle of the position vector of the nucleus, where  $0 < z < a$ . The orientation of the magnetic field,  $\mathbf{B}_0$ , with respect to the  $XYZ$  system, is given by  $[\sin \theta_0 \cos \phi_0, \sin \theta_0 \sin \phi_0, \cos \theta_0]$  ( $\theta_0$  and  $\phi_0$  being the polar and azimuthal angles of  $\mathbf{B}_0$  with respect to the  $XYZ$  system, respectively). The electron–nucleus distance  $r$  is  $r = [\rho^2 + (Z_0 + z)^2]^{0.5}$ . The angle between  $\mathbf{B}_0$  and  $\mathbf{r}$ ,  $\theta$ , is obtained from  $\cos \theta = \mathbf{B}_0 \cdot \mathbf{r} / |\mathbf{B}_0| |\mathbf{r}|$ . Because the positions of the  $^2\text{H}$  nuclei in the layer are not correlated, it is not necessary to consider both  $\phi$  and  $\phi_0$ ; hence, we set  $\phi_0 = 0$ . All possible angles of  $\phi$  were considered in the integration ( $0$ – $360^\circ$ ).

The three-pulse echo intensity for an electron interacting with a single nucleus, neglecting relaxation, is given by<sup>23</sup>

$$V(T) = \frac{1}{2} [V_\alpha(T) + V_\beta(T)] \quad (1)$$

where  $V_\alpha$  and  $V_\beta$  represent contributions from the  $\alpha$  and  $\beta$  spin manifolds, respectively. For  $S = 1/2$  and  $I = 1$ , neglecting the nuclear quadrupole interaction (taken into account later as an additional broadening),<sup>23</sup>

$$V_\alpha(T) = 1 - \frac{16}{3} k \sin^2\left(\frac{\omega_\alpha \tau}{2}\right) \sin^2\left(\frac{\omega_\beta(\tau + T)}{2}\right) + \frac{16}{3} k^2 \sin^4\left(\frac{\omega_\alpha \tau}{2}\right) \sin^4\left(\frac{\omega_\beta(\tau + T)}{2}\right) \quad (2)$$

$$V_\beta(T) = 1 - \frac{16}{3} k \sin^2\left(\frac{\omega_\beta \tau}{2}\right) \sin^2\left(\frac{\omega_\alpha(\tau + T)}{2}\right) + \frac{16}{3} k^2 \sin^4\left(\frac{\omega_\beta \tau}{2}\right) \sin^4\left(\frac{\omega_\alpha(\tau + T)}{2}\right) \quad (3)$$

and

$$k = \left(\frac{\omega_n B}{\omega_\alpha \omega_\beta}\right)^2 \quad \omega_\alpha = \left[\left(\frac{A}{2} + \omega_n\right)^2 + \left(\frac{B}{2}\right)^2\right]^{1/2} \\ \omega_\beta = \left[\left(\frac{A}{2} - \omega_n\right)^2 + \left(\frac{B}{2}\right)^2\right]^{1/2}$$

where  $\omega_n$  is the nuclear Larmor frequency. For weak nonspecific interactions the point dipole approximation applies and

$$A = T_\perp (3 \cos^2 \theta - 1) \quad B = T_\perp (3 \cos \theta \sin \theta) \\ T_\perp = \frac{\mu_0 g_e \beta_e g_n \beta_n}{4\pi \hbar r^3}$$

The echo intensity for an electron spin interacting with  $N$  nuclei in the  $^2\text{H}$  layer is<sup>47</sup>

$$V_N(Z_0, T) = \left[ \frac{1}{2} \prod_{i=1}^N V_\alpha(Z_0, T, i) + \frac{1}{2} \prod_{i=1}^N V_\beta(Z_0, T, i) \right]$$

Because the nuclei's positions are independent, integration can be carried out on each nucleus separately, yielding<sup>18</sup>

$$V_N(Z_0, T) = \frac{1}{2} \left\{ \int_0^{\pi/2} \int_0^{2\pi} \int_0^{40\text{\AA}} \int_0^{a\text{\AA}} V_\alpha(Z_0, \rho, z, \phi, \theta_0) P(\rho) dz d\phi \sin \theta_0 d\theta_0 \right\}^N \\ + \frac{1}{2} \left\{ \int_0^{\pi/2} \int_0^{2\pi} \int_0^{40\text{\AA}} \int_0^{a\text{\AA}} V_\beta(Z_0, \rho, z, \phi, \theta_0) P(\rho) dz d\phi \sin \theta_0 d\theta_0 \right\}^N \\ = \frac{1}{2} [V_\alpha(Z_0, T)]^N + \frac{1}{2} [V_\beta(Z_0, T)]^N \quad (4)$$

where  $P(\rho)$  is the probability of finding the nucleus at  $\rho$  and is given by  $P(\rho) = 2\pi\rho N/V$ , where  $V$  is the volume of the cylinder.

The  $^2\text{H}$  nuclear quadrupole interaction was not taken into account while eq 2 and 3 were derived. Taking it into account would add two more integration parameters, namely, the two Euler angles representing the orientation of the quadrupole principal axis system relative to that of the electron–nucleus dipolar interaction. Averaging over two additional parameters considerably increases the calculation time. Nonetheless, the  $^2\text{H}$  quadrupole interaction does contribute to the ESEEM traces; it is particularly evident for long electron–nuclear distances.<sup>48</sup> Therefore, we accounted for it by introducing an empirical broadening parameter. We multiplied the calculated ESEEM trace (eq 4) by an exponential decay function with a time constant  $T_Q = 1.64 \mu\text{s}$ .  $T_Q$  was obtained by fitting ESEEM traces calculated using eq 4 to ESEEM traces obtained from exact diagonalization of the nuclear Hamiltonian, which includes the quadrupolar interaction (see Supporting Information for details and Figures S2, S3, and S4). The addition of the extra decay yielded an excellent fit up to  $\sim 2.5 \mu\text{s}$ ; thereafter,

there are changes in the modulation phase. In this region, however, the modulation depth is low and within experimental errors.

A value of  $\rho_{\max} = 40 \text{ \AA}$  was obtained by checking for convergence in eq 4. The value used for the layer thickness,  $a$ , was taken from Nagle and co-workers,<sup>49</sup> who reported a headgroup thickness of 9 Å for different phospholipids (DPPC, DMPC, DOPC) in the gel phase (the same value was obtained for the liquid crystalline phase). We took this value because the water and the phospholipid head groups are mixed in the polar interfacial region and the deuterated choline groups can be anywhere within this region. This is also supported by MD simulations<sup>50</sup> that indicated that atoms in lipid bilayers are quite disordered, so the probability distributions for each atom or molecular component has to be taken into account. We also tested  $a$  values of 5 and 7 Å.<sup>18</sup> Here we assumed that by rapid freezing we could preserve the structure of the gel phase. Transition from the gel phase to the subgel phase (below 12 °C) is on the order of several hours;<sup>51</sup> therefore, this assumption is logical.

We set a minimum value of 2.5 Å for  $r$  to account for steric constraints. The upper limit of  $N$  was obtained by dividing the cylinder volume by the volume of three methyl groups.<sup>49</sup> Taking into account the relative content of the deuterated lipid, 70%, and assuming that the two types of lipids are homogeneously mixed yield a maximum  $N$  value of 1762 deuterons ( $d = 39 \text{ N/nm}^3$ ) for  $a = 9 \text{ \AA}$  and  $\rho_{\max} = 40 \text{ \AA}$ . This part of the membrane also contains other molecules and moieties such as water, phosphates, carbonyls, glycerol, and therefore, 1762 is an upper limit.

We also explored the sensitivity of the calculated ESEEM in relation to the size of the cylinder. More specifically, we wanted to determine the distance range that can be probed (Figure S5, Supporting Information). This was achieved by locating an electron spin in the center of the deuterated layer and simulating ESEEM time domain traces for a range of  $\rho_{\max}$  values and plotting  $I(^2\text{H})$  as a function of  $\rho_{\max}$ . Simulations were generated by changing the cylinder radius,  $\rho_{\max}$ , while keeping its thickness,  $a$ , constant or vice versa (Figure S5a,b, Supporting Information). These simulations showed that the model is most sensitive for  $\rho_{\max} < 8 \text{ \AA}$ , in agreement with earlier reports.<sup>18,52</sup> We carried out calculations to verify the validity of the model as a function of  $N$ , which is shown in the Supporting Information, Figure S6. Our model is intended for weak modulation, where the effect of  $N$  can be considered as linear.<sup>18</sup> Finally, the problem of the lack of uniqueness in the best fitted ( $Z_0$ ,  $N$ ) pair is illustrated in Figure S7, Supporting Information.

Initially, we fitted the simulated model to the experimental results using a genetic algorithm to determine  $Z_0$  and  $N$ . The results had different values, depending on the starting values used. Thus, the experimental data were fitted by minimizing the least-squares residuals for each  $Z_0$  and  $N$  pair. The goodness of the least-squares fitting for one ESEEM trace is defined as

$$\chi^2 = \sum_{i=1}^n (V(T)_i - V_N(Z_0, T)_i)^2 \quad (5)$$

where  $n$  is the number of points in the ESEEM trace. We therefore generated 2D plots of  $\chi^2$  vs  $Z_0$  and  $N$ , which were used to choose the best fit range of  $Z_0$  and  $N$ .

**Molecular Modeling.** Molecular modeling was used to obtain dimers of WALP23. The monomer was modeled as a standard  $\alpha$  helix, and two such helices were docked using the

rigid-body geometric-electrostatic version of MolFit.<sup>53,54</sup> Hence, the dimers were evaluated by the geometric and electrostatic complementarity at the monomer–monomer interface. We surmised that electrostatic complementarity is likely to be effective in the hydrophobic environment of the membrane. Hydrophobic complementarity was included in the geometric complementarity term because of the composition of the peptide. A full rotational/translational search was performed with a translational grid interval of 1.05 Å and a rotational interval of 12°, as previously described.<sup>55</sup>

## RESULTS

**CW-EPR Measurements.** Figure 2 shows CW-EPR spectra of singly spin-labeled WALP23 peptides within DPPC/PG

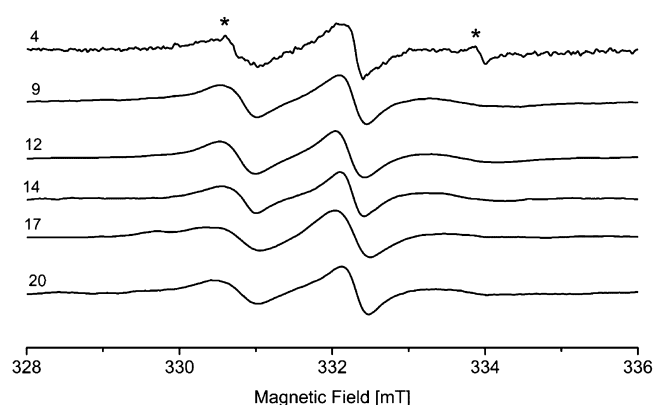


**Figure 2.** CW EPR spectra of WALP peptides labeled at positions 4, 9, 12, 14, 17, and 20 in DPPC/PG (7:3) MLV with D<sub>2</sub>O recorded at ~22 °C. In the WALP23C4 sample there is a small contribution of free MTSL (shown by the asterisks). The EPR spectra were normalized to the maximal amplitude of the  $M_I = 0$  transition.

(7:3) MLV at room temperature (22 °C). The EPR spectra of the labeled WALP23s in the MLV were broadened compared with their spectra in a solution of DMSO (data not shown). This broadening is due to the slower tumbling rate of the peptides when incorporated into DPPC/PG (7:3) MLV and is in agreement with earlier measurements.<sup>56</sup> The S/N of WALP23C4 is lower, probably due to precipitation of the peptide, which caused a low yield.

**ESEEM Measurements.** Figure 3 shows examples of the time domain ESEEM trace and the corresponding FT-ESEEM spectrum of WALP23C20 in frozen suspensions of MLV in D<sub>2</sub>O (a, b) and in MLV prepared from DPPC-*d*<sub>9</sub>/PG (7:3) (c–e). The <sup>2</sup>H signal of the D<sub>2</sub>O sample consists of a narrow component (Figure 3b) owing to remote <sup>2</sup>H nuclei and a broad component because of <sup>2</sup>H nuclei that form H-bonds with the NO group.<sup>43</sup>

In Figure 4a we plotted the dependence of  $I(^2\text{H})$  on the spin label position in WALP23 in DPPC-*d*<sub>9</sub>/PG (7:3) MLV. We observed that  $I(^2\text{H})$  is lowest for WALP23C12, which is situated farthest from the bilayer surface, and is largest for position 20, which is located closest to the surface. As WALP23 crosses the whole bilayer, symmetry about position 12 is expected. While  $I(^2\text{H})$  increases on both sides, the  $I(^2\text{H})$  values are not symmetric, about  $n = 12$ , and showing larger values for  $n > 12$ .

The dependence of  $I(^2\text{H})$  on the spin label position in DPPC/PG MLV in D<sub>2</sub>O is shown in Figure 4b. This plot reflects the water density profile in the membrane and it shows

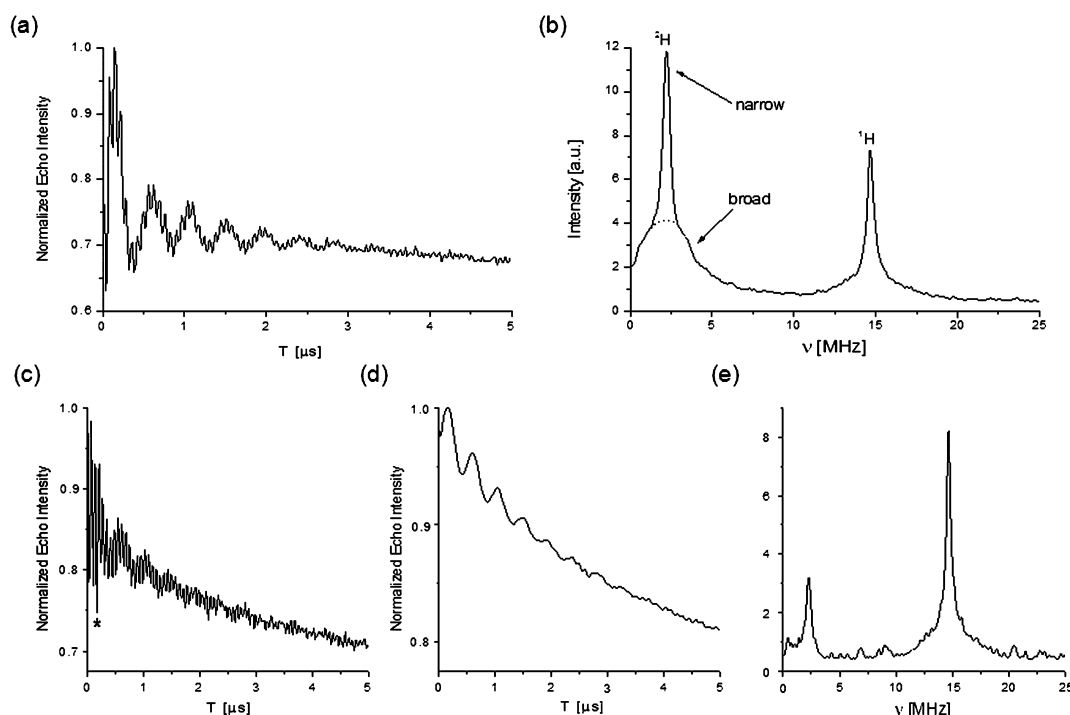


**Figure 3.** (a) Normalized three-pulse ESEEM time domain trace of WALP23C20 in DPPC/PG (7:3) MLV in  $D_2O$ . (b) FT-ESEEM of the trace shown in (a). The narrow and broad components of the  $^2H$  peak are noted on the figure. (c) Normalized three-pulse ESEEM time domain trace of WALP23C20 in DPPC- $d_9$ /PG (7:3) MLV. The asterisk denotes an unwanted echo glitch. (d) Corresponding proton frequency filtered ESEEM trace. (e) FT-ESEEM of the ESEEM trace in (c). For comparison, the  $I(^2H)$  value of the narrow component of a nitroxide spin probe in  $D_2O$  is 33.

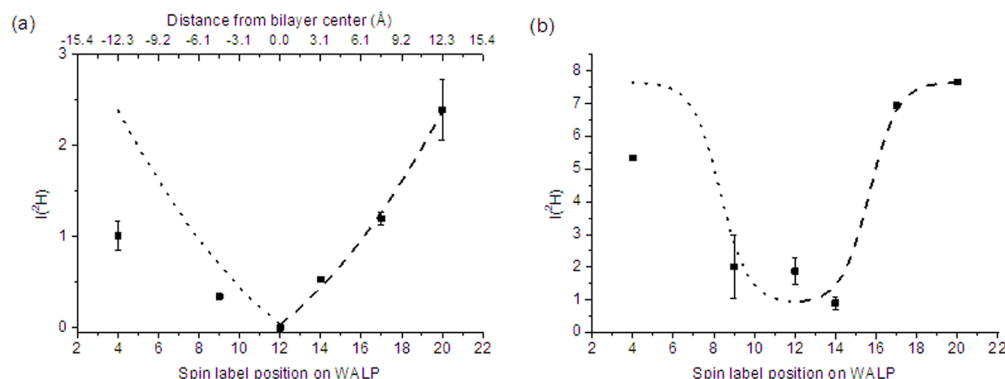


**Figure 4.**  $I(^2H)$  as a function of the spin label position of WALP23 in (a) DPPC- $d_9$ /PG (7:3) MLV and in (b) DPPC/PG (7:3) MLV in  $D_2O$ . The dashed lines denote fits using a second-order polynomial function (in (a)) or a sigmoidal function (in (b)). The lower and upper fitting boundaries represent the ESEEM intensities of positions 12 and 20, respectively. The dotted lines denote the mirror image of the dashed lines. The error bars represent the standard deviation of a duplicate/triplicate of independently prepared samples.

that WALP23C9, 12, and 14 are in a region of low water content, whereas WALP23C20 is situated in a region with the highest water content. The dependence of  $I(^2H)$  on the spin label position is indicative of a sigmoid, with a large derivative at position 16. A similar trend was reported by Marsh and co-workers,<sup>57</sup> where the transmembrane hydrophobicity profile was deduced from oxygen-induced  $T_1$ -relaxation enhancement of spin-labeled lipids. Similarly to the ESEEM results obtained on the DPPC- $d_9$ /PG samples, we observed no symmetry around  $n = 12$ .  $I(^2H)$  is lower than expected for  $n = 4$ , which is symmetric with respect to  $n = 20$ .

To emphasize the observed asymmetric behavior of  $I(^2H)$  in the two types of samples, we fitted the experimental data points for  $n > 12$  to either a second-order polynomial (Figure 4a) or a sigmoid (Figure 4b) and then calculated its mirror image for  $n$

$< 12$ . Figure 4a displays a second X-axis (top) based on the assumption that the depth of the spin label is the same as that of the  $\alpha$ -carbons and that the relative distance between them is that expected from a perfect  $\alpha$ -helix ( $\sim 4.6$  Å). On this scale the zero corresponds to the membrane midplane. According to these assumptions, the  $\alpha$ -carbon in position 4 is placed  $\sim 6$  Å deeper than that of position 20. The results presented in Figure 4 show that the location of the spin label within the membrane can be determined with better resolution from the DPPC- $d_9$ /PG system than from the  $D_2O$  samples because of the sigmoidic shape of the latter. Therefore, we proceeded and analyzed the DPPC- $d_9$ /PG ESEEM data quantitatively using the model we presented earlier.

**Quantitative Analysis of the ESEEM Results of DPPC- $d_9$ /PG.** To obtain the average depth of the spin label in the

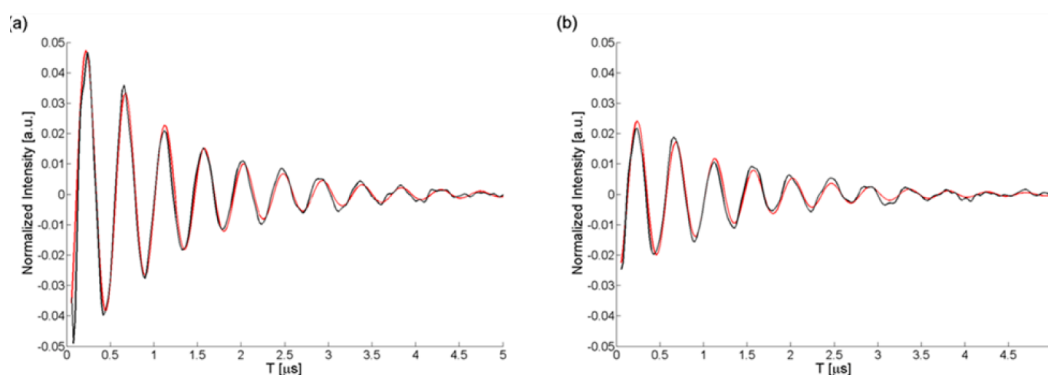


**Figure 5.** Experimental (black) and simulated (red) three-pulse ESEEM of SPCSL in (a) DPPC- $d_9$ /PG (7:3) and in (b) DPPC/DPPC- $d_9$ /PG (3.5:3.5:3). In the simulation  $Z_0 = 3.1$  Å and  $N = 1180$  for (a) and 620 for (b). The data are shown after removing the relaxation decay.

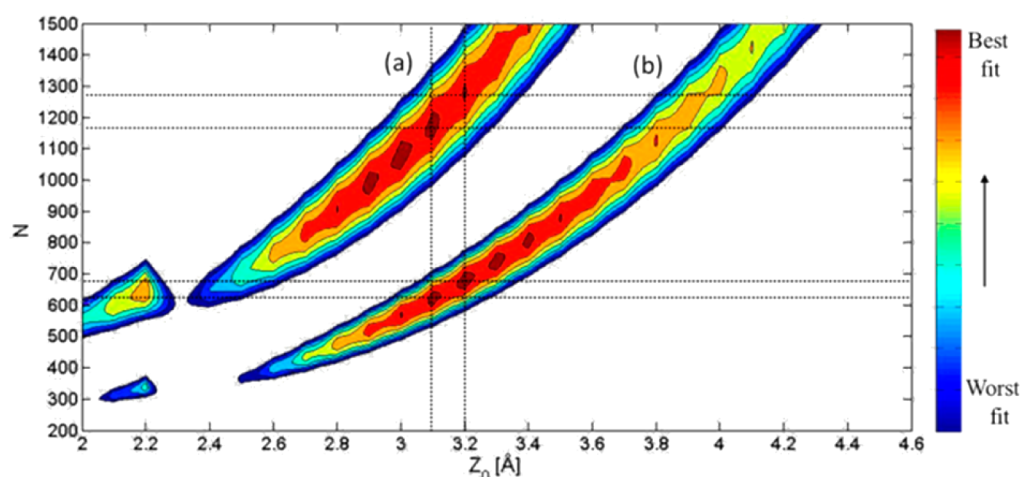


**Figure 6.** Contour plots of  $\chi^2$  for the ESEEM traces of SPCSL in (a) DPPC- $d_9$ /PG (7:3) and in (b) DPPC/DPPC- $d_9$ /PG (3.5:3.5:3). The simulations were done with  $a = 9$  Å. The vertical dashed lines indicate  $Z_0$  values for which  $\chi^2$  values are low for both samples. The horizontal dashed lines represent the range of  $N$  values that correspond to the  $Z_0$  values with minimum  $\chi^2$  values. The color bar is shown on the right. The dark red represents the highest points ( $1 - \chi^2$ ) on the plot (meaning the best fit) and the dark blue represents the lowest points ( $1 - \chi^2$ ) on the plot (meaning the worst fit).

**Table 2. Summary of the Simulations' Best-Fit Parameters for SPCSL**

$a$ , deuterium layer thickness (Å)	$Z_0$ , distance from the deuterium layer (Å)	$N$ , no. of nuclei in the cylinder		$d$ (N/nm <sup>3</sup> )	
		DPPC- $d_9$ /PG (7:3)	DPPC/DPPC- $d_9$ /PG (3.5:3.5:3)	DPPC- $d_9$ /PG (7:3)	DPPC/DPPC- $d_9$ /PG (3.5:3.5:3)
5	$3.15 \pm 0.05$	$770 \pm 30$	$400 \pm 20$	$30.6 \pm 1.2$	$15.9 \pm 0.8$
7	$3.15 \pm 0.05$	$990 \pm 40$	$520 \pm 20$	$28.25 \pm 1.25$	$14.75 \pm 0.55$
9	$3.15 \pm 0.05$	$1220 \pm 45$	$648 \pm 28$	$27 \pm 1$	$14.35 \pm 0.65$

membrane,  $Z_0$ , we fitted the complete experimental time domain ESEEM traces of the spin-labeled WALP23 peptides with the model presented earlier. In addition to  $Z_0$ , the fit also yields the number of deuterium nuclei,  $N$ , in the layer, which in turn yields the  $^2\text{H}$  nuclei density,  $d$ , in the layer. In an earlier work we used this model only to reproduce a single parameter, the modulation depth value, whereas here we fitted the whole time domain trace.<sup>18</sup> Before applying the fitting routine to WALP23 peptides, we tested it on a simple, well-characterized system: a phospholipid spin-labeled at position 5 on the alkyl chain, SPCSL, in the same MLV, namely, DPPC- $d_9$ /PG (7:3) MLV. This is described next.

**Spin-Labeled Phospholipids SPCSL in DPPC- $d_9$ /PG.** Two samples were prepared: SPCSL in MLV of DPPC- $d_9$ /PG (7:3) and DPPC/DPPC- $d_9$ /PG (3.5:3.5:3). These samples

should have the same  $Z_0$  value; however, the  $N$  value of the first sample should be twice that of the second. The ESEEM traces shown in Figure 5 indeed reveal a modulation depth that is about 2-fold smaller for the second sample. We calculated the ESEEM traces for a series of  $Z_0$  and  $N$  values and calculated the  $\chi^2$  values for the two ESEEM traces (Figure 5). These are displayed as contour plots in Figure 6 for  $a = 9$  Å, where the minimum  $\chi^2$  values are presented as the highest points ( $1 - \chi^2$ ) (meaning the best fit). The contour plots of  $1 - \chi^2$  vs  $Z_0$  and  $N$  indicate that there is a very broad maximum with many combinations of  $N$  and  $Z_0$  that provide a good fit (see also Figure S7, Supporting Information). This is an unfortunate characteristic of ESEEM from weakly interacting nuclei. Thus, to select a unique pair, additional constraints are needed. Figure S7 (Supporting Information) shows that for an  $N$  value that is



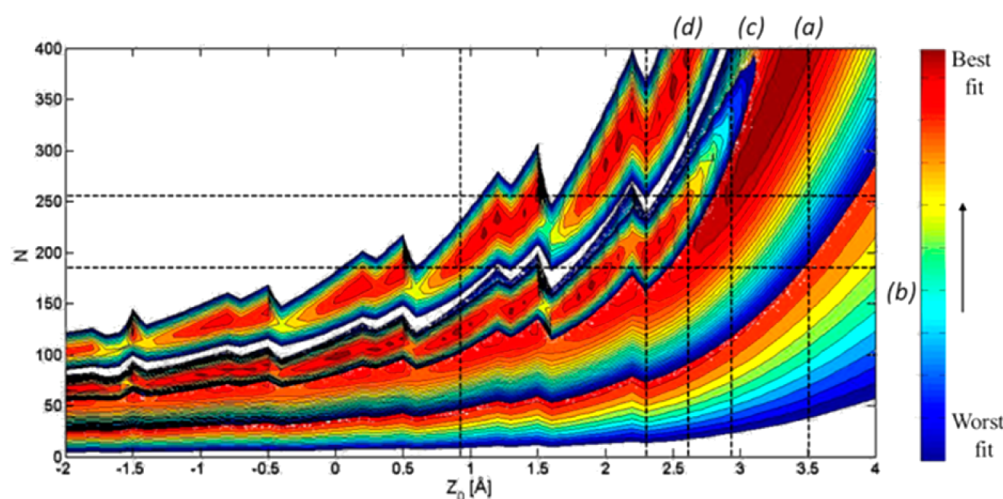


**Figure 7.** Contour plots of  $1 - \chi^2$  for ESEEM traces of (a) WALP23C4, (b) WALP23C14, (c) WALP23C17, and (d) WALP23C20. The simulations were done with  $a = 9$  Å. The horizontal dashed lines indicate  $N$  values for which the  $\chi^2$  value is low for all samples. The vertical dashed lines represent the range of  $Z_0$  values that correspond to  $N$  values with minimum  $\chi^2$  values. Negative values of  $Z_0$  correspond to spin labels located inside the deuterated layer. The contour plot of WALP23C14 is partially masked by that of WALP23C4. The color bar is shown on the right. The dark red represents the highest points ( $1 - \chi^2$ ) on the plot (meaning the best fit) and the dark blue represents the lowest points ( $1 - \chi^2$ ) on the plot (meaning the worst fit).

**Table 3. Summary of the Best-Fit Simulation Parameters Obtained for the Spin-Labeled WALP23 Peptides**

$a$ (Å)	$d$ (N/nm <sup>3</sup> )	$N$	$Z_0$ (Å)			
			WALP23C4	WALP23C14	WALP23C17	WALP23C20
5	$5.56 \pm 0.39$	$140 \pm 10$	$2.85 \pm 0.05$	$3.4 \pm 0.1$	$2.5 \pm 0.1$	$1.3 \pm 0.2$
7	$5.32 \pm 0.49$	$188 \pm 18$	$2.9 \pm 0.1$	$3.4 \pm 0.1$	$2.5 \pm 0.1$	$1.3 \pm 0.2$
9	$4.81 \pm 0.72$	$218 \pm 33$	$2.75 \pm 0.15$	$3.3 \pm 0.2$	$2.45 \pm 0.15$	$1.2 \pm 0.3$

within the density expected in DPPC- $d_9$ /PG, and S/N limitation,  $Z_0 < 6$  Å is the sensitivity limit. Moreover, for  $Z_0 > 4$  Å the uncertainty in  $Z_0$  increases significantly. Therefore, to obtain more experimental constraints, we used two samples with the same  $Z_0$  value and a known ratio of  $N$ , namely, a factor of 2. The vertical lines in Figure 6 indicate the range of  $Z_0$  for which both samples exhibit a minimum  $\chi^2$  value, whereas the horizontal lines denote the corresponding range of  $N$  values. As expected, this shows that the  $N$  value for the spin probe in DPPC- $d_9$ /PG (7:3) is about twice that of DPPC/DPPC- $d_9$ /PG (3.5:3.5:3). For example, a distance of 3.1 Å yields  $N$  values of 1180 and 620 for SPCSL in DPPC- $d_9$ /PG (7:3) MLV and in DPPC/DPPC- $d_9$ /PG (3.5:3.5:3) MLV, respectively. A comparison between the experimental data and the simulation for these values is shown in Figure 5. The  $Z_0$  and  $d$  values extracted from the simulations are summarized in Table 2. Contour plots of  $\chi^2$  for layer thicknesses of  $a = 5$  Å and  $a = 7$  Å are shown in Figures S8 and S9 (Supporting Information) and the parameters extracted are listed in Table 2 as well. They show that whereas  $Z_0$  is not sensitive to  $a$ ,  $d$  is. This reflects the steep dependence of the modulation amplitude on the electron–nuclear distance  $r$  ( $1/r^6$ ) such that only the nuclei in the bottom part of the layer contribute to ESEEM. The values of  $N$  obtained serve as an upper boundary for the number of deuterium nuclei in the polar head region and provide a reference from which the excluded volume effect of the trans-membrane helix and potential local distortions of the lipid layers can be evaluated.

Several methods, including solid-state NMR, fluorescence, and CW-EPR were used to evaluate the membrane depth of spin-labeled phospholipids.<sup>57–61</sup> The average distance between

the DOXYL spin label of SPCSL and phosphate  $^{31}\text{P}$  nuclei in the bilayer polar head region was found to be in the range 10.6–13.6 Å at room temperature.<sup>59,60</sup> It was shown that broad statistical distribution functions have to be taken into account when the  $^{31}\text{P}$  positions in the lipid bilayer are described; its maximum probability is at  $\sim 6$  Å from the bottom of the polar head region.<sup>49</sup>  $Z_0$  corresponds to the distance of the spin label from the bottom of the deuterated choline layer. Accordingly, a distance of  $\sim 3$  Å from the bottom of the deuterated choline layer corresponds to a distance of  $\sim 9$  Å from the average  $^{31}\text{P}$  position. This value is reasonably close to the value of 10.6 Å.<sup>59</sup> Here one has to take into account that the frozen solution reflects the membrane gel phase and not the liquid crystalline phase.<sup>62</sup> This would also lead to some differences between room temperature and low temperature measurements. Next, we proceeded to analyze the ESEEM traces of the WALP23 peptide using this model.

**Spin-Labeled WALP Peptides.** We fitted the ESEEM time domain traces of WALP23C4, 14, 17, and 20, as described earlier. The other samples yielded modulations that were too low. In this analysis we assumed that the  $N$  value is the same for all samples, namely, that the position of the spin label does not affect the density of the deuterated layer in the vicinity of the peptide. Figure 7 shows contour plots of  $1 - \chi^2$  for the ESEEM traces of WALP23C4, 14, 17, and 20 for  $a = 9$  Å. Contour plots for layer thicknesses of 5 and 7 Å are shown in Figures S10 and S11, Supporting Information.

The horizontal dashed lines in Figure 7 indicate the  $N$  values for which the best fit is obtained for all four WALP23 ESEEM traces. The values  $Z_0$  and  $d$ , extracted from the simulations for  $a = 9, 7$ , and 5 Å, are summarized in Table 3. A comparison of



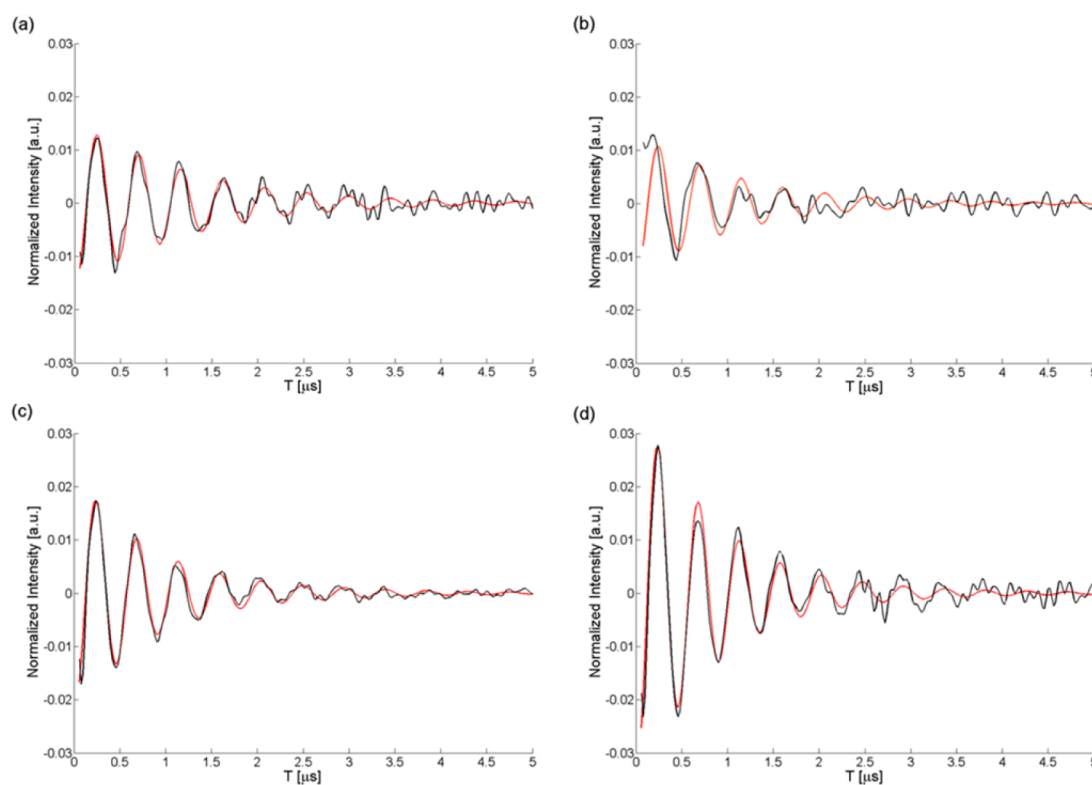


**Figure 8.** Three-pulse ESEEM of WALPs in DPPC- $d_9$ /PG (7:3) MLV: (a) WALP23C4; (b) WALP23C14; (c) WALP23C17; (d) WALP23C20. Simulations (shown in red) obtained using the parameters shown in Table 3 for  $a = 9$  Å. The data are shown after removing relaxation decay.

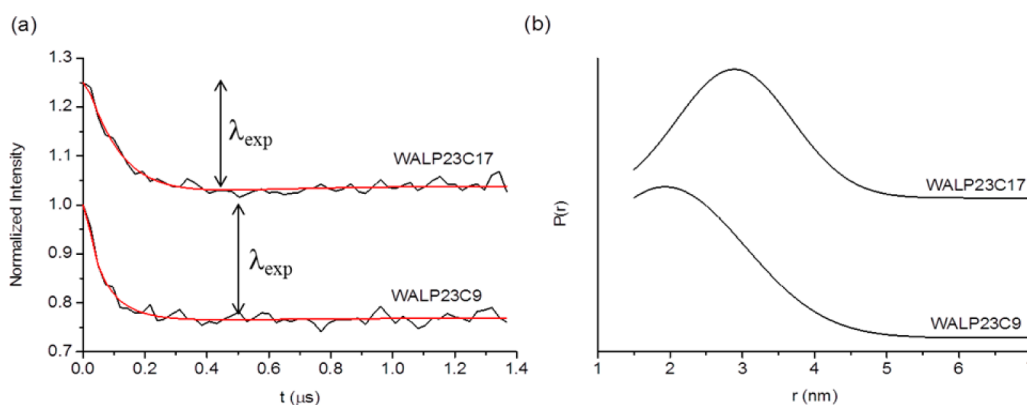


**Figure 9.** DEER traces obtained for WALP23C9 and WALP23C17 in MLV. (a) Background-corrected DEER traces. The red line represents the fit with the distance distribution shown in (b). The traces were normalized to 1 and the trace of WALP23C17 was shifted by 0.25. The experimental modulation depth,  $\lambda_{\text{exp}}$ , is noted on the figure. (b) Corresponding distance distributions obtained by fitting (a) with a single Gaussian.

the experimental data and the simulation with the best fit values obtained for  $a = 9$  Å is shown in Figure 8.

The  $^2\text{H}$  nuclear quadrupole interaction was taken into account as an additional broadening factor. To confirm that this does not affect the distances obtained by the simulations, we carried out simulations for each spin-labeled WALP position using the data in Table 3 with and without the quadrupole interactions (Figure S12, Supporting Information). The differences were small, indicating that the small differences in the  $Z_0$  values of the different spin label positions (Table 3) do not result from neglecting quadrupole interactions.

**DEER Measurements.** The values of  $Z_0$  and  $N$  obtained from fitting the ESEEM traces of WALP23C4, 14, 17, and 20, listed in Table 3, raise two immediate concerns. The first is the

relatively low values of  $N$ , which are  $\sim 5$  times lower than those obtained from SPCSL in the same MLV. Because in an  $\alpha$ -helix all residues point outside of the helix, and considering the distance sensitivity range of  $^2\text{H}$  ESEEM ( $\sim 8$  Å), we expect the excluded volume effect to lead to a reduction of  $\sim 50\%$  in the number of nuclei; a factor of 5 is excessive. The second concern is the small range of distances spanned by the  $Z_0$  values of different spin labels. A difference of about  $\sim 4.6$  Å is expected between the labels at positions 20 and 17, and 17 and 14 if we assume that the spin label is located at the same depth as  $C_\alpha$  (Figure 4, top axis).<sup>27</sup> The simulations yielded differences of only  $\sim 1.2$  and  $\sim 0.9$  Å, respectively.

The low value of  $N$  can be a consequence of peptide oligomerization. Recently, analysis of the broadening effects in

the CW EPR spectra measured at 120 K of spin-labeled WALP23 in the DPPC and DOPC model membranes with peptide/lipid = 1:100, revealed the presence of aggregates.<sup>37</sup> To probe the oligomeric state of WALP23 in our system, we carried out DEER measurements that can provide the distance distribution between the monomers.

Initially we carried out DEER measurements on SPCSL (Figure S13, Supporting Information) as a reference to ensure that the proximity of WALP23 peptides does not occur because of their confinement within the small volume of MLV.<sup>63,64</sup> The data did not reveal the presence of any specific distance and could be fitted by a decay characteristic of a homogeneous distribution according to<sup>65</sup>

$$V(t) = \exp(-kt^{D/3}) \quad (6)$$

where  $V(t)$  is the echo intensity. The dimensionality,  $D$ , obtained from the fit, was 2.3. This dimensionality was used in analyzing the DEER data of the spin-labeled WALP23 peptides. The background decay dimensionality was also fitted independently to the SPCSL sample; the results were in the range 2.1–2.3, which is close to that of the SPCSL sample.

The DEER traces obtained for WALP23C20, 17, 14, 12, and 9 are shown in Figure S14, Supporting Information. Unfortunately, we could not obtain DEER data with a reasonable S/N value for WALP23C4. The DEER traces of the spin labels at positions 9 and 17 showed clear DEER effects and the DEER data after background subtraction are shown in Figure 9 along with the derived distance distributions, which are quite wide,  $2 \pm 1$  and  $3 \pm 1$  nm, respectively. The observed modulation depth,  $\lambda$ , is  $\sim 20\%$  (Figure 9a), which is comparable to the modulation depth we observed recently in doubly labeled melittin in membrane measured under the same experimental conditions.<sup>14</sup> In the case of WALP23C9 it seems that there may be some reduction in the modulation depth due to short interspin distances that cannot be accessed by the pump pulse applied. Interestingly, the DEER trace of WALP23C20 showed no indications of specific spin–spin interactions. We note that we could acquire data only up to 1.4  $\mu$ s, which limits our detection range to maximum distances of  $\sim 4.4$  nm.<sup>11</sup>

It has been shown that the asymptotic value of the echo intensity after background subtraction ( $1 - \lambda_{\text{exp}}$ ), can be used to determine the number of interacting spins,  $N$ , as it is given by  $(1 - \lambda)^{N-1}$ .<sup>66–68</sup>  $\lambda$  is the probability that the pump pulse inverts one spin in a pair. It depends on the actual pulse length used and the nitroxide EPR line shape.<sup>45</sup> Under our experimental conditions  $\lambda \sim 20\text{--}30\%$  and the observed asymptotic values of the echo intensity for WALP23C9 and 17 are 80% (Figure 9a). Accordingly, it is most likely that the dominant oligomers in the sample are dimers, as any higher order oligomers should yield a much larger modulation depth. For example trimers will give a depth of 35–50%. Therefore, a modulation depth of  $\sim 20\%$  suggests that the majority of the oligomers are dimers. However, we cannot exclude the possibility of a distribution of monomers, dimers and trimers, or even higher order oligomers.

The presence of oligomers is also supported by the echo-detected (ED) EPR spectra measured at 50 K (Figure S15, Supporting Information). The derivatives of such spectra, calculated by the application of pseudomodulation<sup>69</sup> are good analogs of the CW EPR spectra. Line broadening due to dipolar interactions are manifested in the increase of the intensity of the low field ( $M_1 = 1$ ) relative to the central field ( $M_1 = 0$ )

spectral components.<sup>70,71</sup> WALP23C9, WALP23C12, and WALP23C17 show increased broadening compared to the other mutants and SPCSL, which is consistent with the DEER data. The  $A_{zz}$  values derived from these spectra do not exhibit any obvious correlation.

The formation of WALP23 oligomers within the membrane accounts for the low value of  $N$  because some of the spin labels can be located at the interface between WALP peptides and, therefore, they are not expected to “encounter” any  $^2\text{H}$  nuclei, thus effectively reducing the value of  $N$ .

## DISCUSSION

In this work we applied  $^2\text{H}$  ESEEM and DEER techniques to obtain the immersion depth of spin labels attached at different positions along the trans-membrane  $\alpha$ -helix peptide WALP23 and its oligomeric state in MLV of DPPC/PG. The following summarizes our results:

- (i) There is an asymmetry in the  $I(^2\text{H})$  values of both  $\text{D}_2\text{O}$  and DPPC- $d_9$  with respect to the center of the WALP23 peptide, position 12.
- (ii) The quantitative ESEEM data analysis revealed an unexpectedly small density of  $^2\text{H}$  nuclei in the polar head region, which is  $\sim 5$ -fold lower than the values obtained for a spin-labeled lipid in the same MLV but without the peptide.
- (iii) The immersion depth values,  $Z_0$ , obtained from simulations of the ESEEM traces yielded a difference of only  $\sim 1.2$  and  $\sim 0.9$  Å between the labels at positions 17 and 20, and 17 and 14, respectively. In an  $\alpha$ -helix the distance between  $\text{C}_\alpha$ 's belonging to residues which are 3 amino acids apart is  $\sim 4.6$  Å.
- (iv) Oligomers, most likely dimers, with distance of  $2 \pm 1$  and  $3 \pm 1$  nm between the spin labels, were observed for WALP23C9 and WALP23C17, respectively. No DEER effect was observed for WALP23C20.

Next, we will discuss the implications of these results in terms of the peptide arrangement in the membrane and the lipid organization around it.

**Asymmetry under Negative Mismatch Conditions.** In an earlier study, Nielsen et al.<sup>27</sup> showed that WALP23 spans the bilayer of DOPC MLV symmetrically, with position 12 being at the bilayer midplane. In this case there is a good match between the WALP23 hydrophobic core and the hydrophobic region of the model membrane. When DOPM was used, a small shift ( $\sim 1$  Å) in the WALP23 center of symmetry was observed. This shift was attributable to the interaction between the electrostatic dipole of WALP23 and the negatively charged lipids. Because of the more electron-deficient C-terminus, the WALP center shift is toward this end.

In contrast to DOPC or DOPM, where there is a good match between the peptide and the lipid bilayer, in DPPC/PG model membranes a negative mismatch is expected because the hydrophobic length of the peptide is shorter than the hydrophobic thickness of the membrane. The hydrophobic stretch of WALP23 is 25.5 Å,<sup>1</sup> whereas the thickness of the hydrocarbon core in a DPPC bilayer in a fully hydrated gel phase was reported to be 34.4 Å<sup>49</sup> and molecular dynamics simulations reported 28.2 Å.<sup>72</sup> The presence of 30% PG is not expected to change this significantly as the alkyl chain length is the same. This yields a negative mismatch of 3–10 Å. Such a mismatch can lead to peptide aggregation, loss of trans-membrane topology, or a reduction in the hydrophobic length

of the phospholipids.<sup>73</sup> It can also affect the order of the acyl chains in the vicinity of the peptide. These phenomena were reported by Rinia et al.,<sup>74</sup> where all WALP16–27 analogs experienced a negative mismatch in the DPPC gel-state bilayers.

Our results indicate that a trans-membrane topology exists with reduced  $I(^2\text{H})$  in the N-terminal side compared with the C-terminal. This suggests that for the WALP23 helix in DPPC/PG (7:3) the center of the helix does not coincide with the lipid bilayer center. Our model membrane also consists of 30% negatively charged lipids, which, as observed by Nielsen et al.,<sup>27</sup> can cause a shift in the helix. Moreover, the WALP23 peptides used in this work were capped only in the peptide C-terminus. Accordingly, under our experimental conditions (pH = 7.2), glycine, which is located at the N-terminus of the peptide, is positively charged. This can induce segregation of the PG lipids near the peptide and enhance the shift toward the C terminus. Figure 10a–c presents schematic illustrations of these effects,

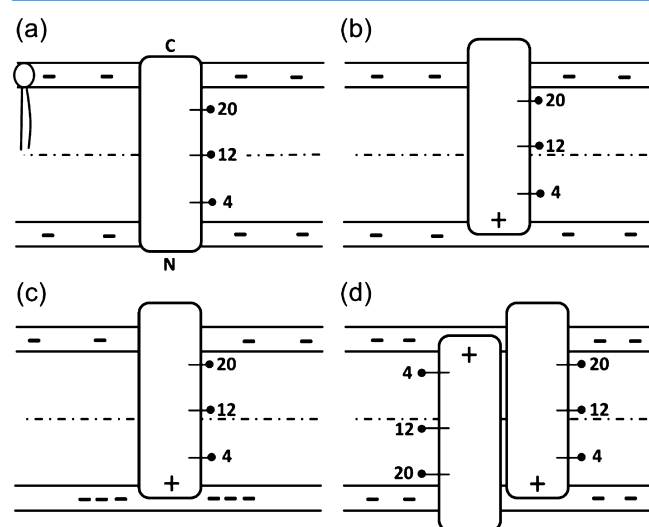


**Figure 10.** Schematic illustrations of spin-labeled WALP23 in a DPPC/PG system. (a) WALP23 crosses the membrane in a symmetric manner. (b) Electrostatic interaction between the PG anionic molecules and the positively charged N-terminus of the peptide causes it to shift toward one edge of the membrane, which leads to a break in the symmetry. (c) Segregation of the phospholipids causes the peptide to shift toward one edge of the membrane. (d) Antiparallel “shifted” arrangement of the WALP dimer causes asymmetry with respect to the peptide center.

assuming that the hydrophilic layer in the peptide region is not distorted. Although the effect of the asymmetry on  $I(^2\text{H})$  is large, the difference in actual depth is small due to the dependence of modulation depth on  $1/r^6$  (Figure S7, Supporting Information).

**Oligomerization of WALP23.** The above arguments account for the observed asymmetry of  $I(^2\text{H})$  with respect to the WALP23 center but do not explain the reduced  $^2\text{H}$  nuclei density in the region of the peptide, as obtained by the simulations. This can be accounted for by the presence of oligomers that were detected by the DEER measurements. The observed oligomerization probably results from the mismatch, as suggested earlier, because it can minimize the distortions exerted on the lipid bilayer by inserting the peptide.<sup>1,6</sup> In oligomers a significant part of the spin labels is expected to point toward the oligomers interface and, therefore, they are

too far from the lipids and do not contribute to  $I(^2\text{H})$ , thus effectively reducing  $N$ .

Although the sample may consist of a distribution of monomers, dimers, trimers, and even higher order oligomers, for simplicity we shall limit our next discussion to the presence of dimers as a representative of the oligomers. Two general types of dimers can be envisioned: in one of them the two  $\alpha$ -helices are parallel and in the second one they are antiparallel. To distinguish between the two possibilities, we made two simple models of a pair of WALP23  $\alpha$ -helices in which we placed cysteines in the positions of the spin labels without the MTSL part (Figure S16, Supporting Information). Next, we measured the relevant cysteine  $C_\beta$ – $C_\beta$  distances (Table 4) and compared them with the experimental distance ranges obtained from the DEER experiments.

**Table 4.** Calculated cysteine  $C_\beta$ – $C_\beta$  Distance in the Various WALP23 Mutants for Parallel and Antiparallel Dimers

WALP23 label position	$C_\beta$ – $C_\beta$ (Å)	
	parallel	antiparallel
20	9.9	21.6
17	8.9	14.3
14	11.2	10.9
12	8.1	9.3
9	10.4	14.5
4	8	28.6

When the distances listed in Table 4 are considered, one must take into account that the spin label–spin label and the  $C_\beta$ – $C_\beta$  distance can differ by as much as 10 Å.<sup>75</sup> In the parallel dimer arrangement all mutants exhibit similar distances, and the distances are rather short, in contrast with the experimental observation. Moreover, the observed distance of  $3 \pm 1$  nm for the WALP23C17 mutant is outside the range predicted by a parallel dimer, including possible elongation due to the MTSL tether. The distances calculated for the antiparallel dimer are in better agreement with the experimental results; they are longer and there is a significant difference between the different constructs, which is in agreement with the experimental observations. Therefore, we find the antiparallel arrangement more likely. The preference of antiparallel dimers for WALP23 in model membranes has already been reported.<sup>76</sup> Although WALP23 dimers or higher aggregations have been detected earlier by other methods,<sup>37,76</sup> using DEER we were able to provide actual distance distributions between the monomers, which can serve as constraints for future modeling.

Next, we will consider whether the presence of antiparallel dimers or oligomers is compatible with the asymmetries observed in the ESEEM data. In the antiparallel arrangement a dimer is electrostatically symmetric with respect to its two ends. Therefore, asymmetry induced by the mechanism driven by the presence of an electrostatic dipole, as shown in Figure 10b,c, can be excluded. In principle, the asymmetry could arise from variations in the degree of burial of the spin labels placed at different positions along the helical chain. Namely, the number of spin labels that point outward or inward with respect to the dimer interface is different and varies along the helix chain. Another possibility is that there is a shift of one monomer with respect to the other, as shown in Figure 10d, where the C terminus is closer to the water interface than to the N terminus. In such an arrangement the spin label attached to cysteine 4 is more buried and “encounters” fewer choline deuterons, or

water molecules. Such an arrangement will also reduce the mismatch with the membrane hydrophobic layer because its effective length is longer than that of the monomer. The preference for the deeper penetration of the N terminus, as opposed to the C-terminus, could be driven by its positively charged  $\text{NH}_3^+$  interacting with the phosphates, as shown in Figure 10b. Finally, we noted that the shift of one monomer with respect to the other will yield longer distances for labels at 20, 17, and 14 and shorter labels at 9 and 4, which is consistent with the experimental results, particularly for WALP23C20, for which we observed no DEER effect. Considering that the mismatch between the hydrophobic cores is  $\sim 3\text{--}10\text{ \AA}$ ,<sup>74</sup> a shift of the C-terminus by  $\sim 3\text{--}10\text{ \AA}$  is needed to “cancel” the mismatch. If we assume that the distances between the spin labels are similar to the distances between the  $\text{C}_\alpha$  along the WALP23  $\alpha$ -helix, then the experimental results indicate a shift of about  $6\text{ \AA}$  (Figure 4), which is within this range.

**Validity of the Model Used To Simulate the ESEEM Time Domain Data.** Although the results of the quantitative ESEEM data analysis, particularly the low  $N$  values obtained, prompted us to think about the presence of oligomers and led to the DEER measurements, we still need to address the question whether the model we used to analyze the ESEEM data is compatible with the presence of WALP23 oligomers. In this work we presented an attempt to use a more realistic model compared to the postulation of an effective electron-nuclei distance and a small effective  $N$  value using the spherical model and at most two shells of nuclei.<sup>77</sup> Unfortunately, the presence of oligomers introduces further complexity in attempting to analyze the ESEEM data quantitatively because there are spin labels located within the interface of the oligomer and these most likely do not “encounter” any deuterium nuclei and consequently do not contribute to the modulation. The relative number of such spin labels may vary throughout the peptide length owing to the shift of the monomers relative to each other. Moreover, the possible presence of monomers should also be considered. Therefore, our assumption that the number of  $^2\text{H}$  nuclei in the layer that is observed by spin labels at different positions is the same is no longer valid. Without such an assumption, or any other experimental constraint, it is impossible to obtain a unique solution for  $Z_0$  and  $N$ , as is obvious from Figure 7. In light of these arguments, the  $Z_0$  and  $^2\text{H}$  density values obtained by fitting the data are ambiguous.

The approach that we used to determine, unambiguously, both the  $Z_0$  and  $N$  values in the case of the spin-labeled phospholipid, where two different membrane deuteration levels were used, is not appropriate for spin-labeled peptides for two reasons. First, it will reduce the modulation depth, which is already rather low. Second, a second parameter that represents the percentage of spin labels that are buried for each spin label position will have to be introduced. This will greatly increase the parameter space and it is not clear whether this will lead to unique solutions and new insights. We believe that the methodology presented will, however, be useful to study the effects of peptides or other additives such as cholesterol on membrane organization using spin-labeled phospholipids, labeled at different places along the alkyl chain.

## SUMMARY AND CONCLUSIONS

The arrangement of the trans-membrane model peptide WALP23 in DPPC/PG model membranes was determined using  $^2\text{H}$  ESEEM and DEER techniques. The  $I(^2\text{H})$  values for the different spin-labeled WALP23 peptides in MLV prepared

in  $\text{D}_2\text{O}$  and with DPPC- $d_9$  lipids indicated that the center of WALP23 does not coincide with the bilayer midplane. The N-terminus was found to be more buried than the C-terminus. Moreover, DEER measurements revealed the presence of WALP23 oligomers, most likely dimers.

An attempt was made to fit the ESEEM data of DPPC- $d_9$  to a model that yields the average distance of the spin label from the membrane deuterated layer,  $Z_0$ , and the density of  $^2\text{H}$  nuclei in this layer,  $d$ . The model was first tested on spin-labeled lipids and it was found that the data can be fitted with a large set of  $Z_0$  and  $d$  pairs, and therefore, additional experimental constraints were necessary to obtain unique parameters. In this particular case this was achieved by measuring a second sample with a different known degree of deuterated lipids in the sample. We applied this methodology to the WALP23 peptides under the constraint that spin labels at different positions experience the same  $d$  value. The data analysis yielded a range of  $d$  values that was unexpectedly low, which we attributed to the presence of oligomers. Although the simple model used for the ESEEM data analysis is valid for spin-labeled lipids and probably also for monomeric peptides, it fails to properly describe a sample with the presence of oligomers.

Comparison of the experimental distance distributions obtained by DEER with distances determined from simplistic models of WALP23 dimers in a parallel and antiparallel configuration suggests that an antiparallel arrangement of the helical monomers is more consistent with the experimental data. Furthermore, to account for the observed asymmetry of  $I(^2\text{H})$ , we suggested that the monomers are shifted with respect to each other, allowing a deeper penetration of the N-terminus. We suggest that the formation of the oligomers is driven by the negative mismatch between the peptide and membrane hydrophobic cores and the electrostatic dipole of the peptide. Such an oligomerization would reduce the bilayer deformation and is therefore considered energetically favorable.

Finally, combining the ESEEM and DEER techniques yielded new quantitative information on the membrane arrangement of the simple well-known WALP23 peptide under conditions of negative mismatch. This methodology can be further applied to study the reciprocal influence of protein/peptides and lipids.

## ASSOCIATED CONTENT

### Supporting Information

LPSVD reconstruction of the three-pulse ESEEM first modulation, calculation of the contribution of the quadrupole interaction as an exponential decay in the ESEEM simulations, an evaluation of the sensitivity range of distances and the range of  $N$  in the theoretical model, a test of the dependence of  $I(^2\text{H})$  on  $Z_0$  for different values of  $N$ , best fit simulations of ESEEM results (contour plots) for  $a = 5, 7\text{ \AA}$ , a test of the effect of neglecting the quadrupole interaction, raw time domain DEER traces obtained for SPCSL and WALP23 peptides in DPPC/PG MLV, low temperature echo-detected EPR spectra of the WALP23 peptides in MLV and molecular modeling showing WALP23 dimer conformations. This material is available free of charge via the Internet at <http://pubs.acs.org>.

## AUTHOR INFORMATION

### Corresponding Author

\*E-mail: [Daniella.goldfarb@weizmann.ac.il](mailto:Daniella.goldfarb@weizmann.ac.il). Phone: +972-8-9342016. Fax: +972-8-9344123.



## Notes

The authors declare no competing financial interest.

## ■ ACKNOWLEDGMENTS

This work was supported by the Israel Science Foundation (ISF). D.G. holds the Erich Klieger Professorial Chair in Chemical Physics. Y.S. is the incumbent of the Harold S. and Harriet B. Brady Professorial Chair in Cancer Research. This research was made possible in part by the historic generosity of the Harold Perlmann Family.

## ■ REFERENCES

- (1) de Planque, M. R. R.; Killian, J. A. *Mol. Membr. Biol.* **2003**, *20*, 271–284.
- (2) Lee, A. G. *Biochim. Biophys. Acta, Biomembr.* **2004**, *1666*, 62–87.
- (3) McIntosh, T. J.; Simon, S. A. *Annu. Rev. Biophys. Biomol. Struct.* **2006**, *35*, 177–198.
- (4) Zhang, W.; Campbell, H. A.; King, S. C.; Dowhan, W. J. *Biol. Chem.* **2005**, *280*, 26032–26038.
- (5) Lee, A. G. *Biochim. Biophys. Acta, Biomembr.* **2003**, *1612*, 1–40.
- (6) Killian, J. A.; Nyholm, T. K. *Curr. Opin. Struct. Biol.* **2006**, *16*, 473–479.
- (7) Glasgow, B. J.; Gasymov, O. K.; Abduragimov, A. R.; Yusifov, T. N.; Altenbach, C.; Hubbell, W. L. *Biochemistry* **1999**, *38*, 13707–13716.
- (8) Oh, K. J.; Zhan, H. J.; Cui, C.; Altenbach, C.; Hubbell, W. L.; Collier, R. J. *Biochemistry* **1999**, *38*, 10336–10343.
- (9) Zhan, H. J.; Oh, K. J.; Shin, Y. K.; Hubbell, W. L.; Collier, R. J. *Biochemistry* **1995**, *34*, 4856–4863.
- (10) Borbat, P.; Freed, J. H. In *Methods Enzymology*; Elsevier: Amsterdam, 2007; *423*, 52–116.
- (11) Jeschke, G.; Polyhach, Y. *Phys. Chem. Chem. Phys.* **2007**, *9*, 1895–1910.
- (12) Schiemann, O.; Prisner, T. F. *Q. Rev. Biophys.* **2007**, *40*, 1–53.
- (13) Borbat, P.; Ramlall, T. F.; Freed, J. H.; Eliezer, D. J. *Am. Chem. Soc.* **2006**, *128*, 10004–10005.
- (14) Gordon-Grossman, M.; Gofman, Y.; Zimmermann, H.; Frydman, V.; Shai, Y.; Ben-Tal, N.; Goldfarb, D. J. *Phys. Chem. B* **2009**, *113*, 12687–12695.
- (15) Herget, M.; Baldauf, C.; Scholz, C.; Parcej, D.; Wiesmuller, K. H.; Tampe, R.; Abele, R.; Bordignon, E. *Proc. Natl. Acad. Sci. U. S. A.* **2011**, *108*, 1349–1354.
- (16) Milov, A. D.; Samoilova, R. I.; Tsvetkov, Y. D.; De Zotti, M.; Toniolo, C.; Raap, J. J. *Phys. Chem. B* **2008**, *112*, 13469–13472.
- (17) Reginsson, G. W.; Schiemann, O. *Biochem. Soc. Trans.* **2011**, *39*, 128–139.
- (18) Carmieli, R.; Papo, N.; Zimmermann, H.; Potapov, A.; Shai, Y.; Goldfarb, D. *Biophys. J.* **2006**, *90*, 492–505.
- (19) Milov, A. D.; Samoilova, R. I.; Tsvetkov, Y. D.; De Zotti, M.; Formaggio, F.; Toniolo, C.; Handgraaf, J. W.; Raap, J. *Biophys. J.* **2009**, *96*, 3197–3209.
- (20) Syryamina, V. N.; Isaev, N. P.; Peggion, C.; Formaggio, F.; Toniolo, C.; Raap, J.; Dzuba, S. A. *J. Phys. Chem. B* **2010**, *114*, 12277–12283.
- (21) Volkov, A.; Dockter, C.; Polyhach, Y.; Paulsen, H.; Jeschke, G. J. *Phys. Chem. Lett.* **2010**, *1*, 663–667.
- (22) Dikanov, S. A.; Tsvetkov, Y. *Electron Spin Echo Envelope Modulation (ESEEM) Spectroscopy*; CRC-Press: Boca Raton, FL, 1992.
- (23) Kevan, L. Modulation of electron spin-echo decay in solids. In *Time Domain Electron Spin Resonance*; John Wiley & Sons: New York, 1979.
- (24) Schweiger, A. G.; Jeschke, G. *Principles of Pulse Electron Paramagnetic Resonance*; Oxford University Press: New York, 2001.
- (25) Volkov, A.; Dockter, C.; Bund, T.; Paulsen, H.; Jeschke, G. *Biophys. J.* **2009**, *96*, 1124–1141.
- (26) Gordon-Grossman, M.; Zimmermann, H.; Wolf, S. G.; Shai, Y.; Goldfarb, D. J. *Phys. Chem. B* **2012**, *116*, 179–188.
- (27) Nielsen, R. D.; Che, K.; Gelb, M. H.; Robinson, B. H. *J. Am. Chem. Soc.* **2005**, *127*, 6430–6442.
- (28) Dzиковski, B.; Tipikin, D.; Freed, J. J. *Phys. Chem. B* **2012**, *116*, 6694–6706.
- (29) Feix, J. B.; Popp, C. A.; Venkataramu, S. D.; Beth, A. H.; Park, J. H.; Hyde, J. S. *Biochemistry* **1984**, *23*, 2293–2299.
- (30) Holt, A.; Killian, J. A. *Eur. Biophys. J.* **2010**, *39*, 609–621.
- (31) Killian, J. A.; Salemin, I.; de Planque, M. R.; Lindblom, G.; Koeppe, R. E., 2nd; Greathouse, D. V. *Biochemistry* **1996**, *35*, 1037–1045.
- (32) Daily, A. E.; Greathouse, D. V.; van der Wel, P. C.; Koeppe, R. E., 2nd. *Biophys. J.* **2008**, *94*, 480–491.
- (33) Beschiaschvili, G.; Seelig, J. *Biochemistry* **1990**, *29*, 52–58.
- (34) Ladokhin, A. S.; White, S. H. *Biochim. Biophys. Acta* **2001**, *1514*, 253–260.
- (35) Papo, N.; Oren, Z.; Pag, U.; Sahl, H. G.; Shai, Y. *J. Biol. Chem.* **2002**, *277*, 33913–33921.
- (36) Papo, N.; Shai, Y. *Biochemistry* **2003**, *42*, 458–466.
- (37) Scarpelli, F.; Drescher, M.; Rutters-Mejneke, T.; Holt, A.; Rijkers, D. T.; Killian, J. A.; Huber, M. *J. Phys. Chem. B* **2009**, *113*, 12257–12264.
- (38) Ren, J.; Lew, S.; Wang, J.; London, E. *Biochemistry* **1999**, *38*, 5905–5912.
- (39) Eibl, H. *Proc. Natl. Acad. Sci. U. S. A.* **1978**, *75*, 4074–4077.
- (40) Fellmann, P.; Zachowski, A.; Devaux, P. F. *Methods Mol. Biol.* **1994**, *27*, 161–175.
- (41) Fauth, J. M.; Schweiger, A.; Braunschweiler, L.; Forrer, J.; Ernst, R. R. *J. Magn. Reson.* **1986**, *66*, 74–85.
- (42) Van Doorslaer, S.; Sierra, G. A.; Schweiger, A. *J. Magn. Reson.* **1999**, *136*, 152–158.
- (43) Erilov, D. A.; Bartucci, R.; Guzzi, R.; Shubin, A. A.; Maryasov, A. G.; Marsh, D.; Dzuba, S. A.; Sportelli, L. *J. Phys. Chem. B* **2005**, *109*, 12003–12013.
- (44) Kumaresan, R.; Tufts, D. W. *IEEE Trans. Acoust., Speech, Signal Process.* **1982**, *30*, 833–840.
- (45) Pannier, M.; Veit, S.; Godt, A.; Jeschke, G.; Spiess, H. W. *J. Magn. Reson.* **2000**, *142*, 331–340.
- (46) Jeschke, G.; Chechik, V.; Ionita, P.; Godt, A.; Zimmermann, H.; Banham, J.; Timmel, C. R.; Hilger, D.; Jung, H. *Appl. Magn. Reson.* **2006**, *30*, 473–498.
- (47) Dikanov, S. A.; Shubin, A. A.; Parmon, V. N. *J. Magn. Reson.* **1981**, *42*, 474–487.
- (48) Milov, A. D.; Samoilova, R. I.; Shubin, A. A.; Grishin, Y. A.; Dzuba, S. A. *Appl. Magn. Reson.* **2008**, *35*, 73–94.
- (49) Nagle, J. F.; Tristram-Nagle, S. *Biochim. Biophys. Acta, Biomembr.* **2000**, *1469*, 159–195.
- (50) Armen, R. S.; Uitto, O. D.; Feller, S. E. *Biophys. J.* **1998**, *75*, 734–744.
- (51) Tristram-Nagle, S.; Wiener, M. C.; Yang, C. P.; Nagle, J. F. *Biochemistry* **1987**, *26*, 4288–4294.
- (52) Cieslak, J. A.; Focia, P. J.; Gross, A. *Biochemistry* **2010**, *49*, 1486–1494.
- (53) Heifetz, A.; Katchalski-Katzir, E.; Eisenstein, M. *Protein Sci.* **2002**, *11*, 571–587.
- (54) Katchalski-Katzir, E.; Shariv, I.; Eisenstein, M.; Friesem, A. A.; Aflalo, C.; Vakser, I. A. *Proc. Natl. Acad. Sci. U. S. A.* **1992**, *89*, 2195–2199.
- (55) Kowalsman, N.; Eisenstein, M. *Bioinformatics* **2007**, *23*, 421–426.
- (56) Freed, H. J. *Spin Labeling Theory and Applications*; Berliner, J. L., Ed.; Academic Press: New York, 1976; 53–132.
- (57) Dzиковski, B. G.; Livshits, V. A.; Marsh, D. *Biophys. J.* **2003**, *85*, 1005–1012.
- (58) Chattopadhyay, A.; London, E. *Biochemistry* **1987**, *26*, 39–45.
- (59) Chu, S. D.; Maltsev, S.; Emwas, A. H.; Lorigan, G. A. *J. Magn. Reson.* **2010**, *207*, 89–94.
- (60) Dalton, L. A.; McIntyre, J. O.; Fleischer, S. *Biochemistry* **1987**, *26*, 2117–2130.

- (61) Strashnikova, N. V.; Medvedeva, N.; Likhtenshtein, G. I. *J. Biochem. Biophys. Methods* **2001**, *48*, 43–60.
- (62) Subczynski, W. K.; Wisniewska, A.; Yin, J. J.; Hyde, J. S.; Kusumi, A. *Biochemistry* **1994**, *33*, 7670–7681.
- (63) Bode, B. E.; Dastvan, R.; Prisner, T. F. *J. Magn. Reson.* **2011**, *211*, 11–17.
- (64) Ruthstein, S.; Potapov, A.; Raitsimring, A. M.; Goldfarb, D. *J. Phys. Chem. B* **2005**, *109*, 22843–22851.
- (65) Milov, A. D.; Tsvetkov, Y. D. *Appl. Magn. Reson.* **1997**, *12*, 495–504.
- (66) Jeschke, G.; Sajid, M.; Schulte, M.; Godt, A. *Phys. Chem. Chem. Phys.* **2009**, *11*, 6580–6591.
- (67) Junk, M. J. N.; Spiess, H. W.; Hinderberger, D. *J. Magn. Reson.* **2011**, *210*, 210–217.
- (68) Milov, A. D.; Ponomarev, A. B.; Tsvetkov, Y. D. *Chem. Phys. Lett.* **1984**, *110*, 67–72.
- (69) Hyde, J. S.; Pasenkiewicz-Gierula, M.; Jesmanowicz, A.; Antholine, W. E. *Appl. Magn. Reson.* **1990**, *1*, 483–496.
- (70) Leigh, J. S. *J. Chem. Phys.* **1970**, *52*, 2608–2612.
- (71) Rabenstein, M. D.; Shin, Y. K. *Proc. Natl. Acad. Sci. U. S. A.* **1995**, *92*, 8239–8243.
- (72) Kandasamy, S. K.; Larson, R. G. *Biophys. J.* **2006**, *90*, 2326–2343.
- (73) Killian, J. A. *Biochim. Biophys. Acta* **1992**, *1113*, 391–425.
- (74) Rinia, H. A.; Kik, R. A.; Demel, R. A.; Snel, M. M. E.; Killian, J. A.; van der Eerden, J. P. J. M.; de Kruijff, B. *Biochemistry* **2000**, *39*, 5852–5858.
- (75) Alexander, N.; Bortolus, M.; Al-Mestarihi, A.; Mchaourab, H.; Meilerl, J. *Structure* **2008**, *16*, 181–195.
- (76) Sparr, E.; Ash, W. L.; Nazarov, P. V.; Rijkers, D. T.; Hemminga, M. A.; Tieleman, D. P.; Killian, J. A. *J. Biol. Chem.* **2005**, *280*, 39324–39331.
- (77) Kevan, L.; Bowman, M. K.; Narayana, P. A.; Boeckman, R. K. *J. Chem. Phys.* **1975**, *63*, 409–416.